JOURNAL OF SYNCHROTRON RADIATION

ISSN 1600-5775

X-ray Laue diffraction by sectioned multilayers. I. *Pendellösung* effect and rocking curves

Vasily I. Punegov*

Institute of Physics and Mathematics, Federal Research Center "Komi Scientific Center", The Ural Branch of the Russian Academy of Sciences, Syktyvkar 167982, Russian Federation.
*Correspondence e-mail: vpunegov@dm.komisc.ru

Received 1 February 2021
Accepted 20 June 2021

Edited by A. Momose, Tohoku University, Japan

Keywords: sectioned multilayers; dynamical X-ray Laue diffraction; recurrence relations; *Pendellösung* effect; rocking curves.

Using the Takagi–Taupin equations, X-ray Laue dynamical diffraction in flat and wedge multilayers is theoretically considered. Recurrence relations are obtained that describe Laue diffraction in structures that are inhomogeneous in depth. The influence of sectioned depth, imperfections and non-uniform distribution of the multilayer period on the *Pendellösung* effect and rocking curves is studied. Numerical simulation of Laue diffraction in multilayer structures W/Si and Mo/Si is carried out. It is shown that the determination of sectioned depths based on the period of the interference fringes of the experimental rocking curves of synchrotron radiation is not always correct.

1. Introduction

Elements of multilayer X-ray optics are widely used in synchrotron radiation installations for transporting X-ray beams (Rack *et al.*, 2010) and focusing radiation (Lyatun *et al.*, 2020), in extreme-ultraviolet lithography (Chkhalo *et al.*, 2017) and in astronomy (Tamura *et al.*, 2018). Such multilayers mainly refer to grazing-incidence reflectors or, in terms of X-ray diffraction in crystals, to Bragg geometry (Authier, 2001).

To focus hard X-rays, it was proposed to create multilayer Laue lenses (Maser *et al.*, 2004), which, like Fresnel zone plates (Kagoshima & Takayama, 2019), transport radiation in transmission geometry. The fabrication of Laue lenses, which are depth-sectioned and thickness-graded multilayers, is a complex problem (Kang *et al.*, 2007). Therefore, the first step in the study of Laue diffraction was presented by a synchrotron X-ray study of laterally bounded (sectioned) multilayers with a constant period (Kang *et al.*, 2004, 2005).

The dynamical theory of X-ray scattering in the Laue case is well developed for crystals, both for symmetric and asymmetric geometry (Authier, 2001). Theoretically, asymmetric diffraction is also possible for sectioned multilayers; however, technologically this is a difficult problem associated with oblique sectioning of a multilayer structure.

Dynamical X-ray Laue diffraction in a multilayer differs compared with diffraction in grazing-incidence geometry. One of the main features is the pendulum (*Pendellösung*) effect (Authier, 2001), when the intensity of the X-ray beam of the transmission wave is transmitted into the diffraction beam and then, with increasing depth, to the contrary, the intensity of the diffraction wave is transmitted into the transmission beam.

In the absence of an algorithm for simulating dynamical Laue diffraction, the analysis of experimental results using the

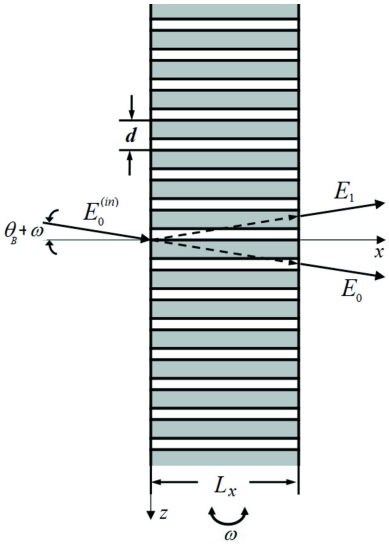

interference-fringe spacing of the rocking curve was not entirely correct (Kang *et al.*, 2005, 2007). Therefore, the present work is devoted to a consistent consideration of the Laue dynamical theory of diffraction in multilayers.

2. Dynamical Laue diffraction in a sectioned multilayer with a constant period

Multilayer Laue lenses are graded multilayers. Unfortunately, on the basis of the Takagi–Taupin equations (Takagi, 1962, 1969; Taupin, 1964; Afanas'ev & Kohn, 1971; Kato, 1973), in the general case, it is impossible to obtain analytical solutions describing Laue diffraction in structures with period variation. Only some laws of changes in the period of the structure allow analytical solutions; in particular, such solutions were previously obtained for crystals with quadratic (Kolpakov & Punegov, 1985) and exponential (Andreev, 2001) displacement fields, and crystals with a transition layer (Chukhovskii & Khapachev, 1985; Kato, 1990). In most cases, one has to limit oneself to the numerical solution of the Takagi–Taupin equations in an oblique coordinate system (Punegov, 2020; Lomov *et al.*, 2021), for example, using the 'half-step derivative' method (Epelboin, 1985).

Therefore, let us consider X-ray dynamical Laue diffraction in a sectioned multilayer with a constant period $d = d_t + d_b$, where d_t is the thickness of the upper layer and d_b is the thickness of the lower layer (Fig. 1).

A plane X-ray wave is incident on the left side of the sectioned multilayer at an angle $\theta = \theta_B + \omega$, where ω is the deviation of the X-ray beam from the Bragg angle θ_B (Fig. 1). In contrast to the Ewald–Laue approach (Authier, 2001), we will proceed from the one-dimensional Takagi–Taupin equations for the periodic structure, which in the Cartesian coordinate system have the form

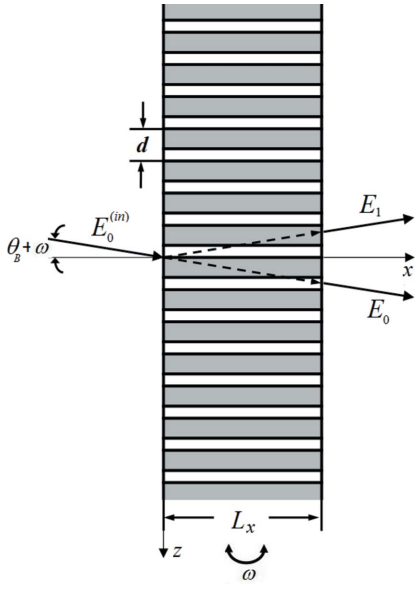

Figure 1
A schematic representation of Laue diffraction by a multilayer. L_x is the sectioned depth and d is the multilayer period.

$$\begin{cases} (\partial/\partial x)E_0(\eta, x) = ia_0E_0(\eta, x) + ia_{-1}f\,E_1(\eta, x), \\ (\partial/\partial x)E_1(\eta, x) = i(a_0 + \eta)E_1(\eta, x) + ia_1f\,E_0(\eta, x), \end{cases} \quad (1)$$

where $E_0(\eta, x)$ and $E_1(\eta, x)$ are the amplitudes of the transmission and diffraction X-ray waves, respectively, $a_0 = \pi\chi_0/(\lambda\cos\theta_B)$, $a_1 = C\pi\chi_1/(\lambda\cos\theta_B)$, $a_{-1} = a_1$, $\eta = 4\pi\sin(\theta_B)\,\omega/\lambda$ is the angular parameter, λ is the wavelength of the X-ray radiation in vacuum, and C is the polarization factor. The Fourier coefficients of the X-ray polarizability for a structure with a two-layer period in the directions of transmission χ_0 and diffraction χ_1 are written as

$$\chi_0 = \frac{\chi_t d_t + \chi_b d_b}{d}, \qquad \chi_1 = \frac{\chi_t - \chi_b}{\pi}\sin\left(\pi\frac{d_t}{d}\right). \quad (2)$$

In relation (2), χ_t and χ_b are the Fourier coefficients of polarizabilities and thicknesses of the upper (t) and lower (b) layers of the period of the multilayer. X-ray polarizabilities of chemical elements are calculated using the tabular values of optical constants: $\chi_j = 2(\delta_j + i\beta_j)$, where $\delta_j = r_0(N_j\lambda^2/2\pi) \times(Z_j + \Delta f_j')$; $\beta_j = -r_0(N_j\lambda^2/2\pi)\Delta f_j''$; j = t or b, which indicates the corresponding layer in the period of the multilayer; $r_0 = e^2/mc^2$ is the classical radius of an electron, where e and m are the charge and mass of an electron, respectively; N_j is the atomic density; Z is the number of electrons in an atom; and $\Delta f_j'$ and $\Delta f_j''$ are dispersion corrections to the atomic amplitude. Equation (1) contains an attenuation factor f, which describes the attenuation of X-ray reflection in a multilayer. This coefficient characterizes the disturbances in the periodic structure of multilayers during their creation. In particular, contribution to the attenuation factor is given by the roughness of the boundaries layers in the structure (Névot & Croce, 1980; de Boer, 1994), errors in layer thickness of the structure (Spiller & Rosenbluth, 1985, 1986), diffusion blurring of boundaries between layers (presence of transition layers) (Stearns, 1989), random loss in a short-period multilayer of a heavy or light layer (Kopylets *et al.*, 2019), local bending of layers during polishing (Kang *et al.*, 2007), *etc.*

For example, accounting for interlayer roughness in Parratt's method of recurrence relations (Parratt, 1954) was considered using the Névot–Croce and Debye–Waller attenuation factors (Bushuev & Sutyrin, 2001; Kohn, 2003). Unfortunately, without an analysis of diffuse scattering, it is difficult to determine the contribution of each type of defect to the attenuation factor. Therefore, in our theoretical consideration of dynamical Laue diffraction, the attenuation factor will take on the value $0 \le f \le 1$ without determining the specific types of defects.

We consider the model generally accepted in the dynamical Laue diffraction theory (Authier, 2001), in which the front of a plane incident X-ray wave and the size of the multilayer are spatially unrestricted in the vertical direction (Fig. 1), hence the amplitudes of X-ray waves in equation (1) depend only on one horizontal coordinate x. Such an X-ray diffraction model can be considered if only the rocking curves are analyzed. In the case where the X-ray beam incident on the multilayer is spatially restricted, it is necessary to use the two-dimensional

Takagi–Taupin equations (Punegov *et al.*, 2017; Punegov & Karpov, 2021). This approach allows one to analyze X-ray reciprocal-space maps (RSMs).

The solution of coupled equation (1) for Laue diffraction can be obtained using the boundary conditions $E_0(\eta, 0) = E_0^{\rm in} = 1$ and $E_1(\eta, 0) = 0$. Applying these boundary conditions, we can obtain expressions for the amplitudes of the transmission $E_0(\eta, x)$ and diffraction $E_1(\eta, x)$ waves,

$$E_0(\eta, x) = \exp(i\psi x)\left[\cos\left(\frac{\xi x}{2}\right) - i\frac{\eta}{\xi}\sin\left(\frac{\xi x}{2}\right)\right] \quad (3)$$

and

$$E_1(\eta, x) = \frac{i2a_1 f \exp(i\psi x)}{\xi}\sin\left(\frac{\xi x}{2}\right), \quad (4)$$

where $\xi = -(\eta^2 + 4f^2 a_1 a_{-1})^{1/2}$ and $\psi = a_0 + \eta/2$.

2.1. *Pendellösung* effect in homogeneous sectioned multilayer

Let us first consider the pendulum (*Pendellösung*) effect under Laue diffraction conditions. If the exact Bragg condition is satisfied ($\eta = 0$) and taking into account $a_1 = a_{-1}$, the intensity distributions of the transmission and diffraction X-ray waves can be written as

$$I_0(x) = \exp(-\mu_0 x)\left[\cos^2(f a_1' x) + \sinh^2(f a_1'' x)\right] \quad (5)$$

and

$$I_1(x) = \exp(-\mu_0 x)\left[\sin^2(f a_1' x) + \sinh^2(f a_1'' x)\right], \quad (6)$$

where $\mu_0 = 2\,{\rm Im}(a_0)$ is the linear coefficient of absorption of X-rays in the multilayer. The dynamical coefficient in equation (1) is represented as $a_1 = a_1' + ia_1''$, where $a_1' = C\pi\chi_1^{\rm r}/(\lambda\cos\theta_{\rm B})$ is a real part and $a_1'' = C\pi\chi_1^{\rm Im}/(\lambda\cos\theta_{\rm B})$ is an imaginary part. Considering $\chi_1^{\rm Im} \ll \chi_1^{\rm r}$ and $|\chi_1| = \chi_1^{\rm r}[1 + (\chi_1^{\rm Im}/\chi_1^{\rm r})^2]^{1/2} \simeq \chi_1^{\rm r}$, solutions (5) and (6) can be rewritten in a more visual form for attenuation *Pendellösung* oscillations as

$$I_0(x) = \exp(-\mu_0 x)\cos^2\frac{\pi x f}{l_{\rm Pen}} \quad (7)$$

and

$$I_1(x) = \exp(-\mu_0 x)\sin^2\frac{\pi x f}{l_{\rm Pen}}. \quad (8)$$

Expressions (7) and (8) clearly describe the *Pendellösung* effect of Laue diffraction when the exact Bragg condition is satisfied. The pendulum beat period $l_{\rm Pen} = \lambda|\cos\theta_{\rm B}|/(C|\chi_1|)$ for a perfect multilayer depends on the Fourier polarizability coefficient χ_1, which characterizes the interaction of X-ray waves in a periodic medium.

Fig. 2 shows the intensity distributions over the depth of a perfect ($f = 1$) Mo/Si multilayer with the same thicknesses of alternating layers, $d_{\rm Mo} = d_{\rm Si} = 3.5$ nm, calculated using exact solutions (5) and (6), as well as using approximate solutions (7) and (8). In the numerical calculations, the synchrotron radiation wavelength $\lambda = 0.1305$ nm was used. The optical constants are presented in Tables 1 and 2. The total depth of the multilayer is $L_x = 2l_{\rm Pen} = 76.4$ µm, which corresponds to

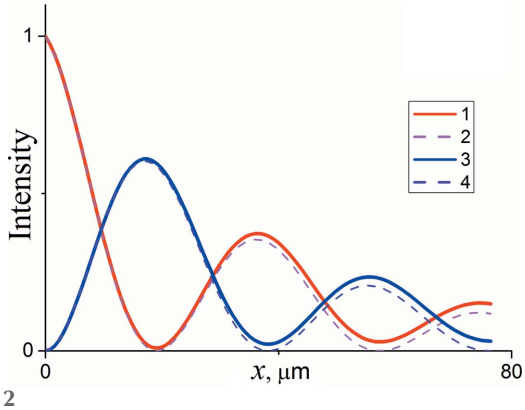

Figure 2
Pendellösung oscillations in an Mo/Si multilayer for transmission (1 and 2) and diffraction (3 and 4) intensities. Curves 1 and 3 were calculated using solutions (5) and (6). Curves 2 and 4 were obtained on the basis of solutions (7) and (8).

two *Pendellösung* distances. At an exact Bragg angle ($\eta = 0$), the transmission intensity at a depth of $x = 19.1$ µm, which corresponds to half the *Pendellösung* distance, almost completely (corrected for photoelectric absorption) transforms into a diffraction wave. Furthermore, the reverse process is observed. The visible difference between the curves of the pendulum effect in the case of exact and approximate solutions is observed at large sectioned depths of the multilayer (Fig. 2).

Fig. 3 demonstrates *Pendellösung* oscillations for a perfect and imperfect Mo/Si multilayer. The attenuation factor for the defect structure is $f = 0.8$. It can be seen from the figure that the period of *Pendellösung* oscillations increases in the case of an imperfect multilayer. This is due to the fact that the presence of defects in the multilayer reduces the reflectivity of the periodic structure. A similar behavior of *Pendellösung* oscillations was observed in the case of dynamical Laue diffraction in a crystal with defects (Punegov & Pavlov, 1992).

Solutions (3) and (4) make it possible to obtain the intensity distributions of the transmission $I_0(x) = |E_0(\eta_\omega, x)|^2$ and diffraction $I_1(x) = |E_1(\eta_\omega, x)|^2$ waves inside the multilayer,

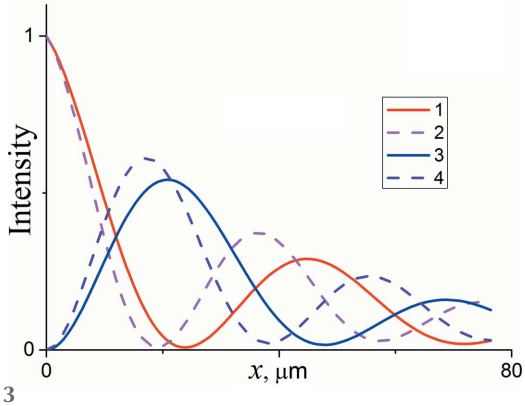

Figure 3
Pendellösung oscillations in an imperfect (curves 1 and 3, attenuation factor is $f = 0.8$) and perfect (curves 2 and 4, $f = 1$) Mo/Si multilayer. Curves 1 and 2 are transmitted intensities, while curves 3 and 4 are diffraction intensities.

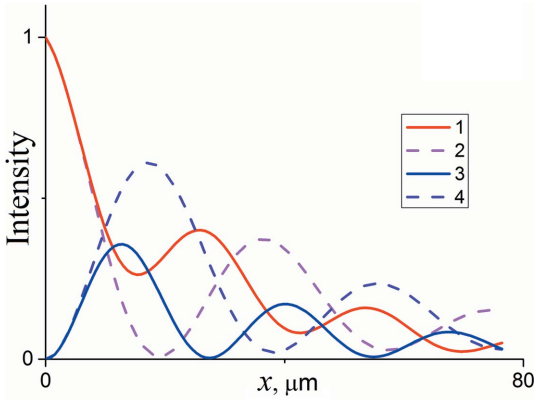

Figure 4
Pendellösung oscillations in an Mo/Si multilayer. Curves 1 and 3 show the calculated transmission and diffraction intensities for $\eta = 0.16$ μm^{-1} ($\omega =$ 0.18 mrad), respectively. Curves 2 and 4 show them for $\eta = 0$.

depending on the value of the angular parameter η (Fig. 4). So, for example, with an angular deviation of the incident X-ray wave from the Bragg angle by $\omega = 0.18$ mrad, a decrease in the period of the *Pendellösung* oscillations is observed (Fig. 4). The transmission X-ray wave is not completely transmitted into the diffraction beam (Fig. 4, curve 3). Therefore, the diffraction intensity inside the multilayer is lower than at the exact Bragg angle (compare curves 3 and 4).

If in equation (1) $a_{-1} = 0$, this means that there is no transfer of intensity from the diffraction beam back to the transmitted beam, solutions (3) and (4) are transformed into expressions corresponding to the kinematical approximation,

$$E_0(\eta, x) = \exp(ia_0 x) \tag{9}$$

and

$$E_1(\eta, x) = ia_1 f \frac{\sin(\eta x/2)}{\eta/2} \exp(i\psi x). \tag{10}$$

In the kinematical approximation, for the intensities of the transmission and diffraction waves, we obtain

$$I_0(x) = \exp(-\mu_0 x) \tag{11}$$

and

$$I_1(x) = \exp(-\mu_0 x)\, a_1^2 f^2 L(\eta x), \tag{12}$$

where $L(\eta x) = \sin^2(\eta x/2)/(\eta/2)^2$ is the Laue interference function (James, 1950). In the case of kinematical diffraction, the intensity of the transmitted wave, according to equation (11), exponentially attenuates due to photoelectric absorption in the multilayer. The intensity of the diffraction wave has a typical angular distribution of kinematical diffraction. Solutions (9)–(12) are valid for multilayers with a very small sectioned depth.

2.2. Rocking curves of a sectioned multilayer with constant period

In experimental works (Kang *et al.*, 2004, 2005, 2007), rocking curves of Laue diffraction from sectioned multilayers are presented as angular dependences of q_x scans in reciprocal space. In our consideration, the deviation from the Bragg angle in solutions (3) and (4) is determined by the parameter η, which corresponds to the q_x scan in reciprocal space (Kang *et al.*, 2005; Punegov *et al.*, 2014, 2016).

In Fig. 5, rocking curves of Mo/Si multilayers of different depths L_x are shown. In the case when the depth of the multilayer is equal to half the *Pendellösung* distance ($L_x = l_{\rm Pen}/2 = 19.1$ μm), the intensity of the diffraction wave, according to Fig. 2, is maximum and is equal to $I_1(\eta = 0) = 0.6\, I_0^{\rm in}$, where $I_0^{\rm in}$ is the intensity of the incident

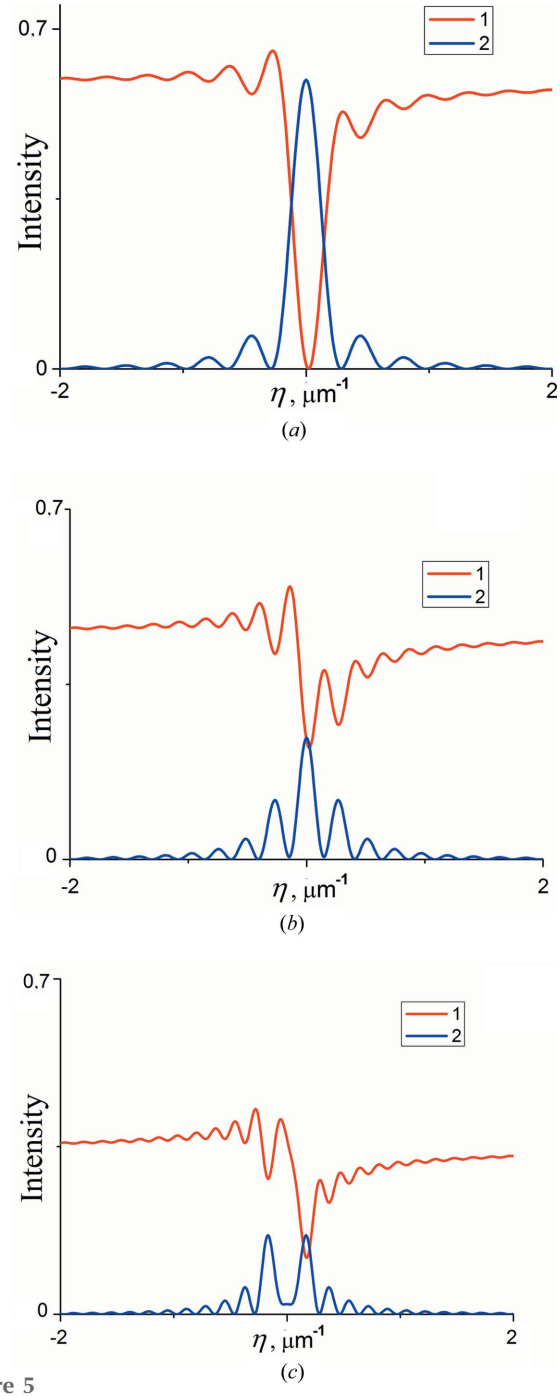

Figure 5
Rocking curves of Laue diffraction depending on the sectional depth L_x of an Mo/Si multilayer. (*a*) $L_x = l_{\rm Pen}/2$, (*b*) $L_x = 3l_{\rm Pen}/4$ and (*c*) $L_x = l_{\rm Pen}$. Curve 1 is transmitted intensity, while curve 2 is diffracted intensity.

radiation. The intensity of the transmitted wave in the exact Bragg orientation is $I_0(\eta = 0) \simeq 0$ [Fig. 5(*a*)].

The rocking curves of the transmitted and diffracted intensities from an Mo/Si multilayer with a depth of $L_x = l_{\rm Pen} \times 3/4 = 28.7$ µm are shown in Fig. 5(*b*). The maximum of the diffracted intensity is $I_1(\eta = 0) = 0.24\, I_0^{\rm in}$. In the case where $L_x = l_{\rm Pen} = 38.2$ µm, the gap is observed in the profile of the rocking curve of the diffraction wave at the exact Bragg orientation [Fig. 5(*c*)] and the minimum of the diffracted intensity is $I_1(\eta = 0) = 5 \times 10^{-6}\, I_0^{\rm in}$. This behavior of the rocking curve is typical for all periodic media in the case of Laue diffraction, when the depth of the sectioned structure is equal to the *Pendellösung* distance.

3. Dynamical Laue diffraction in an inhomogeneous sectioned multilayer: recurrence relations

In addition to flat multilayer Laue lenses, to improve focusing, it has been proposed to manufacture wedged multilayer Laue lenses (Yan *et al.*, 2007; Conley *et al.*, 2008), in which the period of the structure changes not only in thickness z but also along the depth x of the sectioned multilayer system. Equation (1) is written for a multilayer with a constant period and does not allow taking into account the change in the structure period along the x coordinate. A multilayer with wedge layers is a structure whose period varies along the x axis (Fig. 6). Since equation (1) describes diffraction by a structure with a constant period, we divide the wedge multilayer into vertical elementary sections, within which the period of the structure is constant (Fig. 6). We denote the depth of the vertical sections in the direction of the x axis as $x^p - x^{p-1} = l^p$. Here x^p and x^{p-1} are the coordinates of the left and right boundaries of the vertical elementary section with a number p, respectively, and l^p is the depth of this section, while the sections are numbered from left to right (p = 0, 1, 2, ..., P). The superscript of all

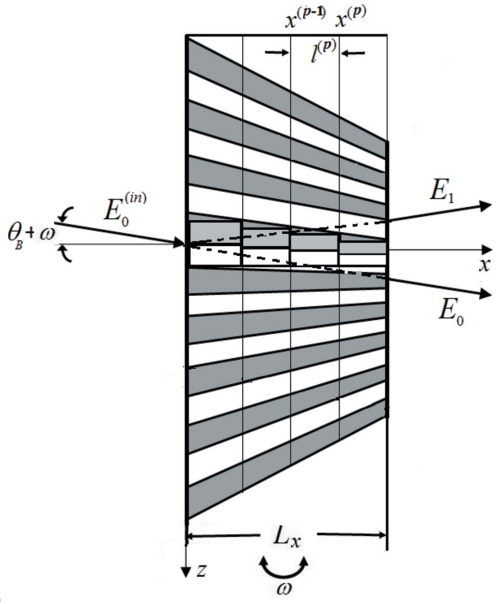

Figure 6
A schematic representation of X-ray Laue diffraction in a wedge multilayer.

parameters corresponds to the elementary section number. Let the diffraction in the first vertical section be described by equation (1), then for the section with the number p instead of the parameter η in (1) one should write $\eta^p = \eta + \Delta\eta^p$, where $\Delta\eta^p = 2\pi\, \Delta d^p/d^2$ and $\Delta d^p = d - d^p$ is the mismatch of the period of the pth vertical elementary section relative to the first vertical section with a multilayer period $d^1 = d$.

X-ray diffraction in the pth elementary vertical section of the multilayer is described by a system of equations of the form

$$\begin{cases} \partial E_0^p(\eta, x)/\partial x = i a_0\, E_0^p(\eta, x) + i a_{-1} f^p\, E_1^p(\eta, x), \\ \partial E_1^p(\eta, x)/\partial x = i(a_0 + \eta + \Delta\eta^p)\, E_1^p(\eta, x) + i a_1 f^p\, E_0^p(\eta, x). \end{cases} \tag{13}$$

Let $E_0^{p-1}(\eta, x^{p-1})$ and $E_1^{p-1}(\eta, x^{p-1})$ represent the amplitudes of the X-ray fields at the boundary $(p-1)$ of the pth vertical elementary section. Then, taking into account these boundary conditions, we can obtain solutions for the transmission and diffraction waves inside the elementary section with number p,

$$E_0^p(\eta, x) = B_1^0 \exp\left[i\xi_1^p\left(x - x^{p-1}\right)\right] - B_2^0 \exp\left[i\xi_2^p\left(x - x^{p-1}\right)\right] \tag{14}$$

and

$$E_1^p(\eta, x) = B_1^1 \exp\left[i\xi_1^p\left(x - x^{p-1}\right)\right] - B_2^1 \exp\left[i\xi_2^p\left(x - x^{p-1}\right)\right], \tag{15}$$

where

$$\xi_1^p = \frac{(2a_0 + \eta^p) - \left[\left(\eta^p\right)^2 + (f^p)^2 4a_1 a_{-1}\right]^{1/2}}{2},$$

$$\xi_2^p = \frac{(2a_0 + \eta^p) + \left[\left(\eta^p\right)^2 + (f^p)^2 4a_1 a_{-1}\right]^{1/2}}{2},$$

$$\xi^p = \xi_1^p - \xi_2^p = -\left[\left(\eta^p\right)^2 + (f^p)^2 4a_1 a_{-1}\right]^{1/2},$$

$$\varphi_1^0 = \frac{a_0 - \xi_2^p}{\xi^p},$$

$$\varphi_2^0 = \frac{a_0 - \xi_1^p}{\xi^p},$$

$$\varphi_1^1 = \frac{a_0 + \eta^p - \xi_2^p}{\xi^p},$$

$$\varphi_2^1 = \frac{a_0 + \eta^p - \xi_1^p}{\xi^p},$$

$$B_{1,2}^0 = \varphi_{1,2}^0 E_0^{p-1}(\eta, x^{p-1}) + \frac{a_{-1}\, E_1^{p-1}(\eta, x^{p-1})}{\xi^p}$$

and

$$B^1_{1,2} = \varphi^1_{1,2} E_1^{p-1}(\eta, x^{p-1}) + \frac{a_{-1}\, E_0^{p-1}(\eta, x^{p-1})}{\xi^p}.$$

At the boundary between the pth and the $(p + 1)$th elementary vertical sections, the solutions for the amplitudes of X-ray waves have the form

$$E_0^p(\eta, x^p) = B_1^0 \exp(i\xi_1^p l^p) - B_2^0 \exp(i\xi_2^p l^p) \qquad (16)$$

and

$$E_1^p(\eta, x^p) = B_1^1 \exp(i\xi_1^p l^p) - B_2^1 \exp(i\xi_2^p l^p). \qquad (17)$$

The amplitudes $E_0^p(\eta, x^p)$ and $E_1^p(\eta, x^p)$ serve as the boundary conditions for diffraction in the $(p + 1)$ elementary vertical section. Performing sequentially the procedure of recurrent calculations with the initial boundary conditions on the input face, $E_0^0(\eta, x^0) = 1$ and $E_1^0(\eta, x^0) = 0$, we obtain the amplitudes of the transmitted $E_0^P(\eta, x^P)$ and diffracted $E_1^P(\eta, x^P)$ waves on the output face of the multilayer inhomogeneous in depth L_x, where $L_x = \sum_{p=0}^{P} l^p$.

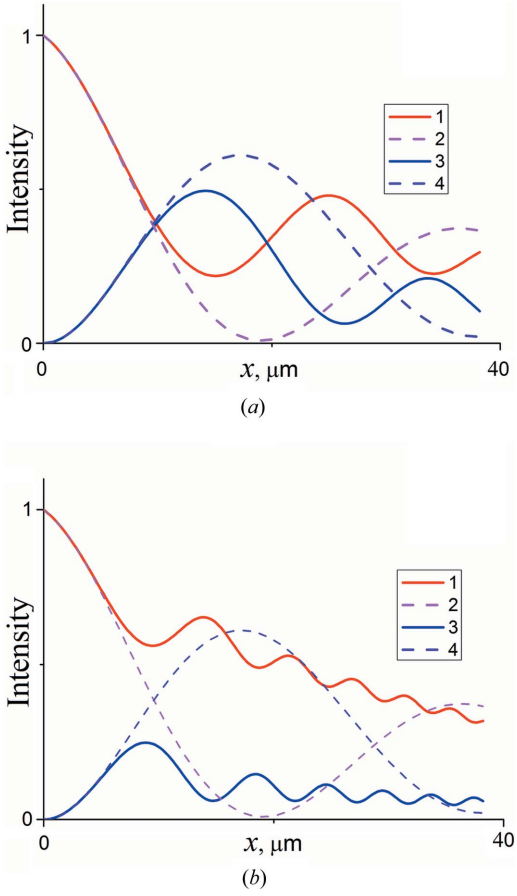

Figure 7
Distributions of transmitted (curve 1) and diffracted (curve 3) intensities inside an Mo/Si multilayer with weak (*a*) and strong (*b*) gradients of period variation. Curves 2 and 4 correspond to a perfect Mo/Si multilayer with a constant period. The number of elementary vertical sections for a wedge multilayer is $P = 200$.

3.1. *Pendellösung* effect in the case of a wedge sectioned multilayer

To calculate the intensity distribution of the transmission and diffraction waves in the wedge multilayer (Fig. 6), we used the recurrence relations (16) and (17). We will consider cases of weak and strong linear period variation. In the first case, the period varies with the depth of the Mo/Si multilayer from 7.000 to 6.997 nm. In the case of a strong gradient, the period changes from 7.000 to 6.986 nm. Fig. 7 shows the depth distributions of intensities in Mo/Si multilayers with variations in the periods. In the case of a weak gradient of the period variation at the initial depth interval from 0 to 10 μm, the behavior of the transmission and diffraction intensities coincides with the *Pendellösung* effect of a multilayer with a constant period. Furthermore, due to the gradient of the period variation of the Mo/Si system, the classical *Pendellösung* effect is violated. As a result, the distance of the *Pendellösung* fringe decreases and the intensity of the transmission wave is not completely transferred to the diffraction beam [Fig. 7(*a*)]. For a strong gradient of the period variation of the Mo/Si multilayer, the *Pendellösung* profiles of the transmission and diffraction X-ray waves do not intersect. The period of the *Pendellösung* fringe decreases monotonically with the depth of the sectioned multilayer [Fig. 7(*b*)].

The intensity distributions of the transmission and diffraction waves also depend on the lateral disturbance gradient of the multilayer structure. The *Pendellösung* effect depending on the weak and strong gradient of the attenuation factor is shown in Fig. 8. The attenuation factor varies linearly from 1 to 0.8 in the case of a weak gradient and from 1 to 0.6 in the case of a strong gradient. Since the perfection of the multilayer structure deteriorates along the depth of the Mo/Si multilayer, the period of *Pendellösung* oscillations in the direction of the x axis increases. We see that the stronger the attenuation-factor-variation gradient, the more visible the increase in the *Pendellösung* distance along the depth of the multilayer (Fig. 8).

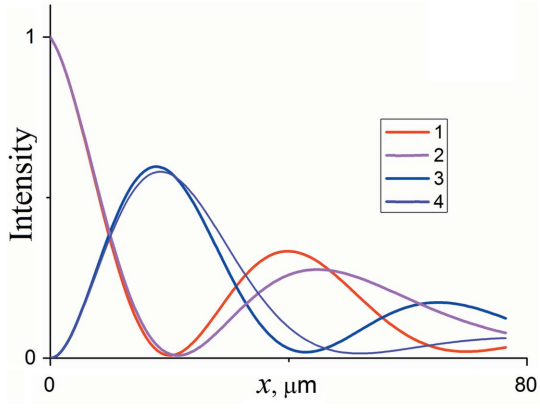

Figure 8
Distributions of transmitted (curves 1 and 2) and diffracted (3 and 4) intensities inside an Mo/Si multilayer with weak (1 and 3) and strong (2 and 4) attenuation-factor gradients. The number of elementary vertical sections is $P = 200$.

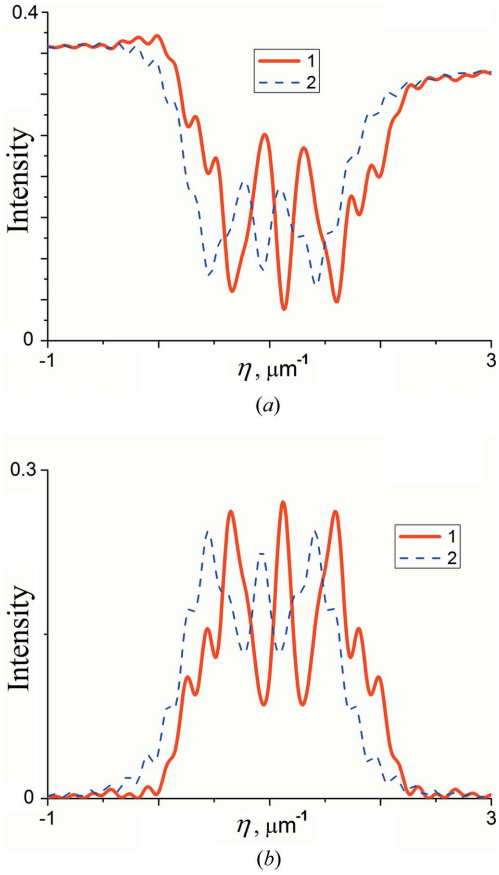

Figure 9
Rocking curves of the transmitted (*a*) and diffracted (*b*) waves in the case of a strong period-variation gradient of Mo/Si multilayer for different numbers of fragmentations P into elementary vertical sections. Curve 1 corresponds to fragmentation $P = 4$, while curve 2 refers to the case where $P = 30$. $L_x = l_{Pen} = 38.2$ μm.

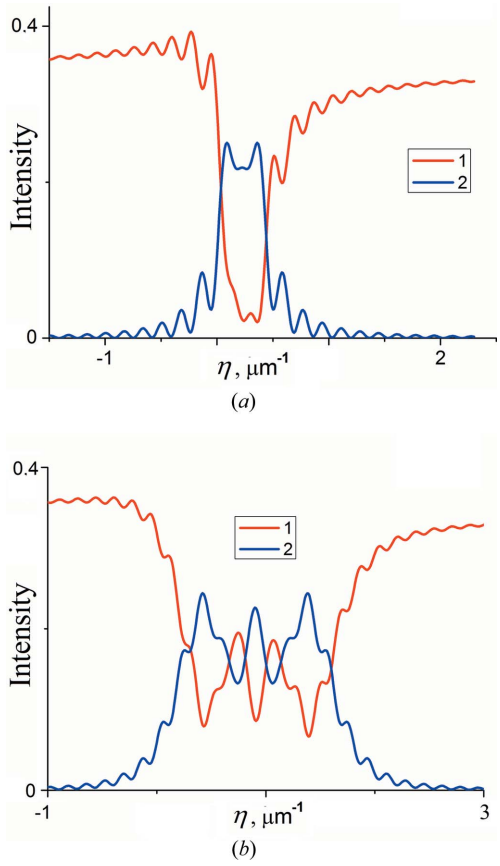

Figure 10
Rocking curves of transmitted (curve 1) and diffracted (curve 2) waves from an Mo/Si multilayer with weak (*a*) and strong (*b*) gradients of period variation. The number of elementary vertical sections is $P = 300$, while the sectioned depth of the multilayer is $L_x = l_{Pen} = 38.2$ μm.

3.2. Rocking curves of wedge sectioned multilayers

We calculated X-ray rocking curves of Mo/Si multilayers that are nonuniform over depth x ($L_x = l_{Pen} = 38.2$ μm) using the recurrent solutions (16) and (17). In Fig. 9, the rocking curves of transmission and diffraction waves with the strong variation gradient of the multilayer period for different numbers of fragmentations P of the structure depth into elementary vertical sections are shown. Starting from $P = 30$, an increase in the number of fragmentations into elementary sections does not change the rocking-curve profile.

Fig. 10 demonstrates the rocking curves of wedge Mo/Si multilayers with weak and strong gradients of period variation along the depth of the sectioned structure. On the profile of the rocking curve of the diffracted wave in the case of the weak gradient, a gap is observed [Fig. 10(*a*)], which is less deep compared with the splitting of the rocking curve of a flat multilayer [Fig. 5(*c*)]. The rocking curve of the multilayer with the strong period-variation gradient has two symmetrical gaps [Fig. 10(*b*)].

The influence of linearly varying attenuation factors along the depth of the sectional Mo/Si multilayer with a constant period d on the profiles of the rocking curves is shown in Fig. 11. The weak gradient of the attenuation-factor variation insignificantly affects the rocking curves [compare Fig. 11(*a*) with Fig. 5(*c*)]. On the other hand, a strong attenuation-factor gradient strongly changes the profile of the diffraction curve [Fig. 11(*b*)].

4. Determination of the depth of sectioned multilayers

An experimental study of Laue diffraction in sectioned W/Si and Mo/Si multilayers with hard synchrotron radiation energies (9.5 and 19.5 keV) was performed for sectioned depths from 2 to 17 μm (Kang *et al.*, 2005). The period of the W/Si multilayer was 29 nm (sample A). The volume fraction of tungsten in the W/Si period was 60%. The second Mo/Si structure had a period of 7 nm with an equal proportion of Mo and Si (sample B). Since in the article (Kang *et al.*, 2005) the results of diffraction were mainly discussed using synchrotron radiation with a wavelength of $\lambda = 0.1305$ nm (energy $E = 9.5$ keV), in this work numerical calculations were performed using this wavelength for structures A and B.

The optical constants of tungsten, molybdenum and silicon with respect to the wavelength $\lambda = 0.1305$ nm of synchrotron radiation were obtained using the *X-ray Server* computer program (Stepanov, 1997, 2013; Stepanov & Forrest, 2008),

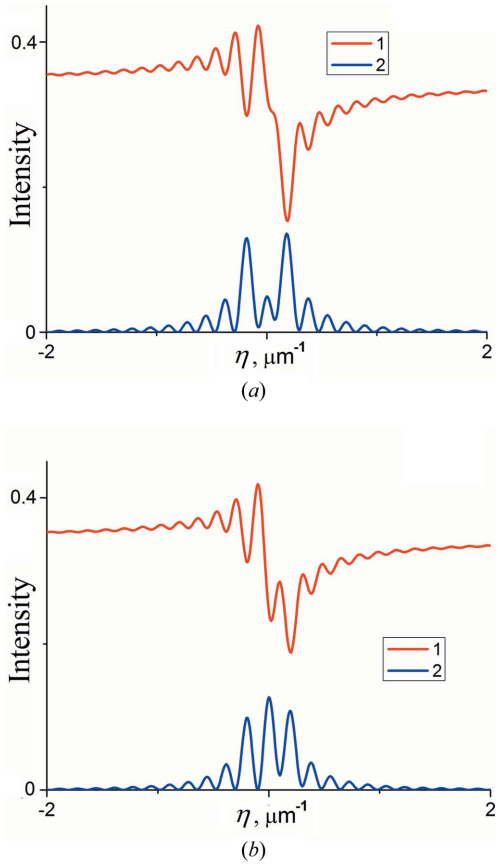

Figure 11
Rocking curves of transmitted (curve 1) and diffracted (curve 2) waves from an Mo/Si multilayer with weak (*a*) and strong (*b*) attenuation-factor gradients. The number of elementary vertical sections is $P = 300$, while the sectioned depth of the multilayer is $L_x = l_{\rm Pen} = 38.2$ μm.

and are shown in Table 1. Based on these data, the Fourier coefficients of X-ray polarizability, χ_0 and χ_1, for the case of Laue diffraction in W/Si and Mo/Si multilayers, were calculated (Table 2).

The *Pendellösung* distance for the W/Si multilayer is more than four times less than the corresponding value for the Mo/Si structure ($l_{\rm Pen}^{\rm MoSi/Si} = 38.2$ μm). There are two options for determining the sectioned depth of multilayers L_x. The first approach is based on the fact that the depths of the sectioned multilayers L_x are determined by measuring the period of interference fringes on the rocking-curve profile. There are two drawbacks to this approach. First, this method is precisely realized within the kinematical approximation. Second, good angular resolution is needed in the measurement of the rocking curves. The second approach is based on the numerical simulation of the rocking curves for Laue diffraction from multilayers using dynamical diffraction solutions. Even with the absence of information on the structural perfection of multilayers, the second approach gives an insignificant error in numerical simulation and subsequent comparison with experimental measurements.

For a synchrotron radiation energy of 9.5 keV in the Laue diffraction experiment involving W/Si and Mo/Si multilayers,

Table 1
Optical constants of silicon, molybdenum and tungsten at a synchrotron radiation wavelength λ = 0.1305 nm.

Material	Density (gm cm^{-3})	Energy (keV)	Fourier coefficients of X-ray polarizability χ_j ($\times 10^{-5}$)
Si – amorphous	2.0	9.5	−0.219 + *i* 0.00089
Mo – amorphous	4.5	9.5	−1.783 + *i* 0.08958
W – amorphous	19.0	9.5	−6.279 + *i* 0.37728

Table 2
Fourier coefficients of X-ray polarizability of Mo/Si and W/Si multilayers at a synchrotron radiation wavelength λ = 0.1305 nm.

Multilayer	d (nm)	λ (nm)	$\theta_{\rm B}$ (mrad)	χ_0 ($\times 10^{-5}$)	χ_1 ($\times 10^{-5}$)
Mo/Si	7	0.1305	2.25	−1.465 + *i* 0.058	−0.341 + *i* 0.0267
W/Si	29	0.1305	9.32	−4.152 + *i* 0.228	−1.626 + *i* 0.107

the angular distribution of the scattered intensity was investigated by scanning the scattering vector in the direction of the projection Q_x (Kang *et al.*, 2005), which corresponds to the angular parameter $\eta = Q_x$ in our consideration. The W/Si and Mo/Si samples were wedge shaped in the y direction perpendicular to the diffraction plane (x, z), which gave a change in the sectioned depth L_x. The rocking curves were calculated using solution (4) for the diffracted wave.

As in the experimental work (Kang *et al.*, 2005), in the numerical simulation, we used the W/Si structure with a period $d = d_{\rm W} + d_{\rm Si} = 29$ nm, where $d_{\rm W} = 17.4$ nm and $d_{\rm Si} = 11.6$ nm. In the case of the Mo/Si multilayer, the period was $d = d_{\rm Mo} + d_{\rm Si} = 7$ nm with $d_{\rm Mo} = d_{\rm Si} = 3.5$ nm. The optical constants of these multilayers are presented in Table 2.

It is known that the rocking-curve profiles always have a gap when the sectional depth of the sample is close to the *Pendellösung* distance (Authier, 2001). The calculated X-ray rocking curves of the sectioned W/Si and Mo/Si multilayers for different depths are shown in Fig. 12.

For W/Si multilayers with depths L_x equal to 2.6, 4.4, 6.6 and 8.8 μm, the calculated rocking curves [Fig. 12(*a*)] are close to the experimental data (Kang *et al.*, 2005), with the characteristic gap in the profile of the diffraction curve appearing for $L_x = 8.8$ μm ($l_{\rm Pen}^{\rm W/Si} = 8.01$ μm). For a relatively large depth $L_x = 10.7$ μm, the calculated rocking curve differs from the experimental diffraction curve (Kang *et al.*, 2005).

The diffraction curves of the Mo/Si multilayers with small sectioned depths of 3.9, 6.3 and 8.6 μm [Fig. 12(*b*)] are consistent with experimental data (Kang *et al.*, 2005). However, the calculated rocking curves for sectioned depths of 11.2 and 15.0 μm [Fig. 12(*b*)] differ significantly from the experimental results (Kang *et al.*, 2005). For example, the experimental diffraction curve from an Mo/Si multilayer with a depth of 15.0 μm has a gap in the middle of the rocking-curve profile. Such a gap is only possible when the sectional depth L_x is close in value to the *Pendellösung* distance ($l_{\rm Pen}^{\rm MoSi/Si} = 38.2$ μm). Thus, analysis of experimental data to

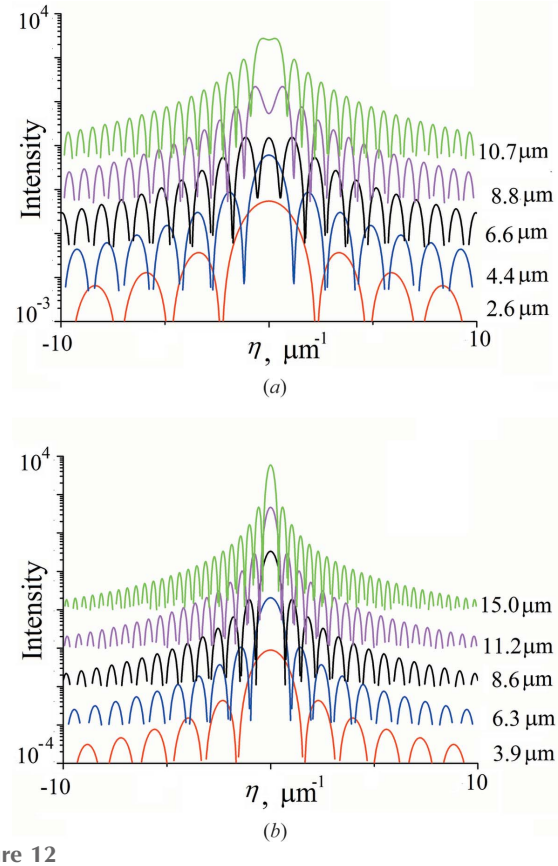

Figure 12
Calculated diffraction rocking curves in the Laue geometry from W/Si (*a*) and Mo/Si (*b*) multilayers with different sectioned depths L_x. The diffracted intensities are offset by factors of 10^2 for clarity.

determine the sectioned depth $L_x^{\eta_0} = 2\pi/\eta_0$ (Kang *et al.*, 2005) using the value of the interference-fringe spacing η_0 is not always justified. For example, for the depth $L_x = 15.0$ μm and $\eta_0 = 0.42$ μm^{-1}, and for $L_x = 38.2$ μm and $\eta_0 = 0.165$ μm^{-1}.

The question then arises: why for small sectioned depths of multilayers are the calculated and experimental rocking curves close to each other, but for large L_x they are significantly different? Fig. 13 shows the calculated rocking curves of the Mo/Si multilayer structure for the sectioned depth L_x = 38.2 μm with different angular resolutions. We also show the influence of the instrumental function on X-ray diffraction from multilayers in the Laue geometry (curves 2, Fig. 13). In our calculations, we used a diffraction scheme containing a four-bounces Ge(220) monochromator and a three-bounces Ge(220) analyzer.

In the case of a large depth L_x, interference oscillations are located close to each other; therefore, all oscillations are observed only at a high angular resolution $\Delta\eta = 0.02$ μm^{-1} [Fig. 13(*a*)] and the period of oscillations is $\eta_0 = 0.1646$ μm^{-1}. In the case of a low resolution, for example, $\eta_0 = 0.335$ μm^{-1}, not all interference oscillations are registered; therefore, in this case, the distance between the oscillations is η_0 = 0.335 μm^{-1} [Fig. 13(*b*)]. From this value, we can obtain the sectioned depth $L_x = 18.8$ μm, which is approximately two times less than in the case of high angular resolution. Consequently, the analysis of the experimental data of X-ray Laue diffraction to determine the sectional depth of multilayer structures is possible only under the condition of a high angular resolution of the rocking curves.

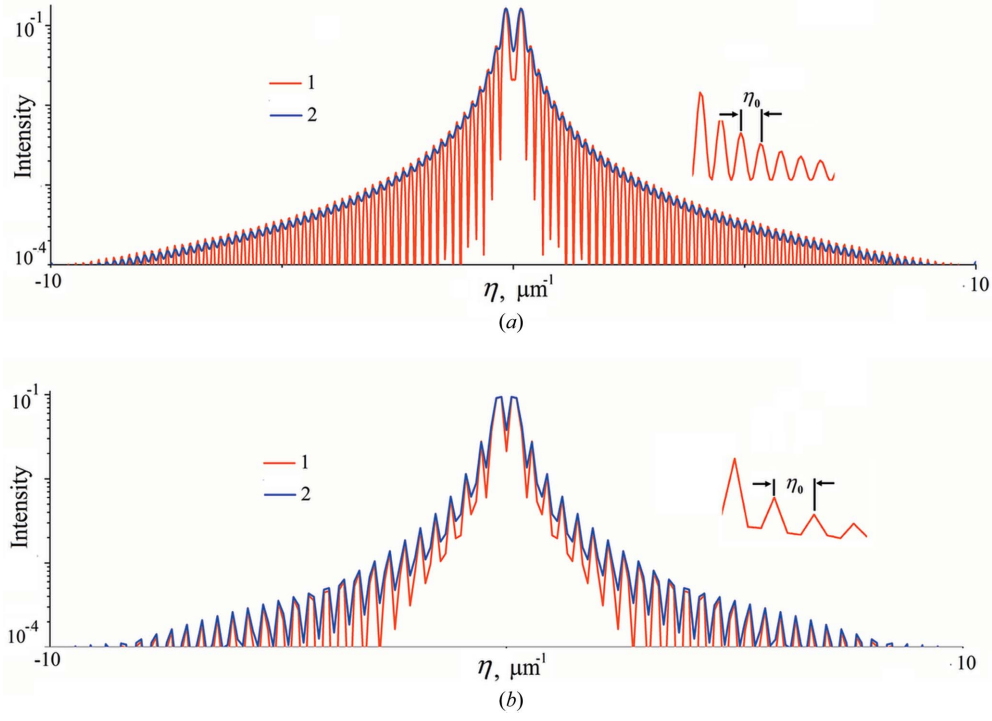

Figure 13
Calculated rocking curves (curve 1) from an Mo/Si multilayer with sectioned multilayer depth $L_x = l_{Pen} = 38.2$ μm. The diffraction curves (curve 2) are also presented, taking into account the instrumental function. The angular resolutions (*a*) are $\Delta\eta = 0.02$ μm^{-1} and (*b*) $\Delta\eta = 0.1$ μm^{-1}, while the periods of the interference fringes are (*a*) $\eta_0 = 0.1646$ μm^{-1} and (*b*) $\eta_0 = 0.335$ μm^{-1}.

5. Concluding remarks

We have theoretically investigated in detail X-ray Laue diffraction in multilayers in the case of an incident plane wave. The influence of sectional depth, imperfections (defects) and non-uniform distribution of the period of multilayers on the *Pendellösung* effect and rocking curves has been shown. However, more complete information on the structure of multilayers is provided by the use of triple-axis diffractometry (Iida & Kohra, 1979; Punegov, 2015). Therefore, the next step will be to consider the Laue diffraction in the case of restricted X-ray beams (Punegov *et al.*, 2017; Punegov & Karpov, 2021). This will make it possible to calculate RSMs in Laue geometry, as well as compare the calculated q_x and q_z sections of RSMs with experimental data (Kang *et al.*, 2005).

References

Afanas'ev, A. M. & Kohn, V. G. (1971). *Acta Cryst.* A**27**, 421–430.
Andreev, A. V. (2001). *JETP Lett.* **74**, 6–9.
Authier, A. (2001). *Dynamical Theory of X-ray Diffraction.* Oxford University Press.
Boer, D. K. G. de (1994). *Phys. Rev. B*, **49**, 5817–5820.
Bushuev, V. A. & Sutyrin, A. G. (2001). *Surf. Investig.* **16**, 121–126.
Chkhalo, N. I., Gusev, S. A., Nechay, A. N., Pariev, D. E., Polkovnikov, V. N., Salashchenko, N. N., Schäfers, F., Sertsu, M. G., Sokolov, A., Svechnikov, M. V. & Tatarsky, D. A. (2017). *Opt. Lett.* **42**, 5070–5073.
Chukhovskii, F. N. & Khapachev, Yu. P. (1985). *Phys. Status Solidi A*, **88**, 69–76.
Conley, R., Liu, C., Qian, J., Kewish, C. M., Macrander, A. T., Yan, H., Kang, H. C., Maser, J. & Stephenson, G. B. (2008). *Rev. Sci. Instrum.* **79**, 053104.
Epelboin, Y. (1985). *Mater. Sci. Eng.* **73**, 1–43.
Iida, A. & Kohra, K. (1979). *Phys. Status Solidi A*, **51**, 533–542.
James, R. W. (1950). *The Optical Principles of the Diffraction of X-rays.* London: G. Bell and Sons.
Kagoshima, Y. & Takayama, Y. (2019). *J. Synchrotron Rad.* **26**, 52–58.
Kang, H. C., Stephenson, G. B., Liu, C., Conley, R., Khachatryan, R., Wieczorek, M., Macrander, A. T., Yan, H., Maser, J., Hiller, J. & Koritala, R. (2007). *Rev. Sci. Instrum.* **78**, 046103.
Kang, H. C., Stephenson, G. B., Liu, C., Conley, R., Macrander, A. T., Maser, J., Bajt, S. & Chapman, H. N. (2004). *Proc. SPIE*, **5537**, 127–132.
Kang, H. C., Stephenson, G. B., Liu, C., Conley, R., Macrander, A. T., Maser, J., Bajt, S. & Chapman, H. N. (2005). *Appl. Phys. Lett.* **86**, 151109.
Kato, N. (1973). *Z. Naturforsch.* **28**, 604–609.
Kato, N. (1990). *Acta Cryst.* A**46**, 672–681.
Kohn, V. G. (2003). *Poverkhnost*, **1**, 23–27.
Kolpakov, A. V. & Punegov, V. I. (1985). *Solid State Commun.* **54**, 573–578.
Kopylets, I., Devizenko, O., Zubarev, E., Kondratenko, V., Artyukov, I., Vinogradov, A. & Penkov, O. (2019). *J. Nanosci. Nanotechnol.* **19**, 518–531.
Lomov, A. A., Punegov, V. I. & Seredin, B. M. (2021). *J. Appl. Cryst.* **54**, 588–596.
Lyatun, I., Ershov, P., Snigireva, I. & Snigirev, A. (2020). *J. Synchrotron Rad.* **27**, 44–50.
Maser, J., Stephenson, G. B., Vogt, S., Yun, W., Macrander, A., Kang, H. C., Liu, C. & Conley, R. (2004). *Proc. SPIE*, **5539**, 185–194.
Névot, L. & Croce, P. (1980). *Rev. Phys. Appl. (Paris)*, **15**, 761–779.
Parratt, L. G. (1954). *Phys. Rev.* **95**, 359–369.
Punegov, V. I. (2015). *Phys. Usp.* **58**, 419–445.
Punegov, V. I. (2020). *JETP Lett.* **111**, 376–382.
Punegov, V. I. & Karpov, A. V. (2021). *Acta Cryst.* A**77**, 117–125.
Punegov, V. I., Kolosov, S. I. & Pavlov, K. M. (2014). *Acta Cryst.* A**70**, 64–71.
Punegov, V. I., Kolosov, S. I. & Pavlov, K. M. (2016). *J. Appl. Cryst.* **49**, 1190–1202.
Punegov, V. I. & Pavlov, K. M. (1992). *Sov. Tech. Phys. Lett.* **18**, 390–391.
Punegov, V. I., Pavlov, K. M., Karpov, A. V. & Faleev, N. N. (2017). *J. Appl. Cryst.* **50**, 1256–1266.
Rack, A., Weitkamp, T., Riotte, M., Grigoriev, D., Rack, T., Helfen, L., Baumbach, T., Dietsch, R., Holz, T., Krämer, M., Siewert, F., Meduňa, M., Cloetens, P. & Ziegler, E. (2010). *J. Synchrotron Rad.* **17**, 496–510.
Spiller, E. & Rosenbluth, A. E. (1985). *Proc. SPIE*, **0563**, 221–236.
Spiller, E. & Rosenbluth, A. E. (1986). *Opt. Eng.* **25**, 954–963.
Stearns, D. G. (1989). *J. Appl. Phys.* **65**, 491–506.
Stepanov, S. (2013). *J. Phys. Conf. Ser.* **425**, 162006.
Stepanov, S. A. (1997). *X-ray Server*, https://x-server.gmca.aps.anl.gov/.
Stepanov, S. & Forrest, R. (2008). *J. Appl. Cryst.* **41**, 958–962.
Takagi, S. (1962). *Acta Cryst.* **15**, 1311–1312.
Takagi, S. (1969). *J. Phys. Soc. Jpn*, **26**, 1239–1253.
Tamura, K., Kunieda, H., Miyata, Y., Okajima, T., Miyazawa, T., Furuzawa, A., Awaki, H., Haba, Y., Ishibashi, K., Ishida, M., Maeda, Y., Mori, H., Tawara, Y., Yamauchi, S., Uesugi, K. & Suzuki, Y. (2018). *J. Astron. Telesc. Instrum. Syst.* **4**, 011209.
Taupin, D. (1964). *Bull. Soc. Fr. Miner. Crist.* **87**, 469–511.
Yan, H. F., Maser, J., Macrander, A., Shen, Q., Vogt, S., Stephenson, G. B. & Kang, H. C. (2007). *Phys. Rev. B*, **76**, 115438.